

Image Blurring Effects Due to Depth Discontinuities: Blurring that Creates Emergent Image Details*

Thang C. Nguyen and Thomas S. Huang

Email: cthang@uirvld.csl.uiuc.edu, huang@uicsl.csl.uiuc.edu

Beckman Institute and Coordinated Science Laboratory

405 N. Mathews Street, Urbana, IL 61801, USA

Abstract: A new model (called multi-component blurring or MCB) to account for image blurring effects due to *depth discontinuities* is presented. We show that blurring processes operating in the vicinity of large depth discontinuities can give rise to emergent image details, quite distinguishable but nevertheless un-explained by previously available blurring models. In other words, the maximum principle for scale space [Per90] does not hold. It is argued that blurring in high-relief 3-D scenes should be more accurately modeled as a multi-component process. We present results from extensive and carefully designed experiments, with many images of real scenes taken by a CCD camera with typical parameters. These results have consistently support our new blurring model. Due care was taken to ensure that the image phenomena observed are mainly due to de-focussing and not due to mutual illuminations [For89], specularity [Hea87], objects' "finer" structures, coherent diffraction, or incidental image noises. [Gla88] We also hypothesize on the role of blurring on human depth-from-blur perception, based on correlation with recent results from human blur perception. [Hes89]

Keywords: Multi-component image blurring (MCB), depth-from-blur, point-spread functions (kernels), incoherent imaging of 3-D scenes, human blur perception, active vision.

1 Introduction

The objectives of this paper are: to present a simplified image blurring model that is sufficiently general to account for blurring effects due to depth discontinuities, and to explore some implications on depth-from-blur techniques. See [Ens91], [Gar87], [Gro87], [Pen87&89], [Sub88a], and many others. Previously none of those known depth-from-blur formulations discussed such important cases. We realized that an accurate model must be composite (i.e. consisting of a possibly unknown number of sub-processes.) The composite nature of blurring due to depth-discontinuities give rise to the net blurring effects, with new local extrema generated, very much in discord with commonly employed blurring models.

The organization of this paper is as follows:

Section 2 discusses the radiometry of image formation in the presence of sharp discontinuities. Only incoherent (or very weakly coherent), polychromatic lighting was assumed to be present (this was enforced in the experiments), as is often true in normal, everyday lighting, thus radiometric models approximate the imaging process adequately. These simple radiometric considerations are then seen to be capable of predicting blurring instances in which interesting resultant image structures (emergent details like peaks and valleys) are created. The object-and-camera configuration used in this analysis is also adapted to the real-scene experiments presented in section 3.

Section 3 presents the results from extensive experiments with images of realistic scenes taken with a Cohu-4815 CCD camera with 8-bit accuracy. Temporal averaging over twenty frames each image was employed to subdue various image noises to

* This work is supported by the National Science Foundation under the Creativity in Engineering Award EID-8811553, and grant IRI-89-02728

about one gray level in variance. Various settings of camera parameters (focal length f , aperture D and back-focal distance v) are employed to test the blurring model. Also, controlled experiments for checking ground truth were performed to ensure valid interpretation.

In section 4 we illustrate the implications for depth-from-blur, an active vision algorithm suitable for close range. We simulated Pentland's "localized power estimation" algorithm [Pen89] to estimate the blur widths for simple (single-component) blurring profiles as well as multi-component blurring (MCB) cases. Finally we discuss implications to the modeling of human monocular depth perception. This last discussion could suggest further psychophysical investigation.

2 Modeling of Single-component and Multi-component Blurring

2.1 Image blur as a function of depth

Blurring (MCB or otherwise) herein always means de-focussing instead of diffraction blurring (which does not contribute significantly in our problems.) With a simple blend between geometrical and radiometric optics, the width w_i of a normalized, positive blurring kernel can be defined as: (similar to [Sub88b])

$$\langle w_i^2 \rangle \triangleq \int_{-\infty}^{\infty} \int_{-\infty}^{\infty} (X - \bar{X})^2 K_i(X) dX; \quad \bar{X} = \int_{-\infty}^{\infty} \int_{-\infty}^{\infty} X K_i(X) dX \quad (1)$$

and this width is linearly related to the the blur circle diameter, $D|v_i - v_0|/v_0$, and inversely to the depth (distance) u_i :

$$w_i \simeq \kappa D \frac{|v_i - v_0|}{v_0} = \kappa D \frac{f|u_i - u_0|}{u_0(u_i - f)}; \quad \text{from the lens equation: } \frac{1}{f} = \frac{1}{u_i} + \frac{1}{v_i} \quad (2)$$

where κ is a small constant, f is focal length, u_i is distance from the point P_i to first principal plane of the lens system, and v_i is that distance from the second principal plane to the plane of best focus for p_i , image of point P_i . If u_0 is set at infinity (farther objects in better focus), then the relation above is simplified to:

$$w_i \simeq \kappa D \frac{f}{u_i - f}; \quad \text{when } u_0 \rightarrow \infty \quad (3)$$

giving only one solution. So, focusing camera at infinity is desirable to prevent ambiguities in depth-from-blur. We will assume such a setting henceforth.

2.2 Image formation across depth discontinuities

Figure 1 represents a simplified model of a camera imaging a sharp edge that "just cut" onto the optical axis and standing in front of a uniform background. The Lambertian assumption, though convenient, is not required, only that no specular reflection, no significant mutual illumination effects (interreflections) are present in the scene, and negligible image noise. Care must be exercised to prevent the aforementioned effects since they sometimes create spurious image features that can be confused with multi-component blurring effects. [For89], [Hea87] Note that a knife-sharp edge is *not* necessary here (as would be required in monochromatic

coherent diffraction experiments) and the real "edge" used was just a *carefully hand-cut* edge (by a sharp blade) out of a high-quality foam-filled cardboard. In fact, it is our objective to show that MCB effects are detectable in scenes containing realistic objects.

This is perhaps the most important point of this paper: image blurring near a depth discontinuity can be best analyzed separately for each surface patch at different depth. We will concentrate on the cases where one of the blurring process is *dominant* (i.e. having a much larger spread than others) in the image neighborhood. (For example, in figure 1 the blurring due to \mathbf{E} , the edge, is dominant.)

Toward modeling the imaging process of a 3-D scene, [Fri67] found that the transfer function for a 3-D object cannot be *cascaded*. For example, in the case of a 3-D object imaged by a cascade of two lens systems. The transfer function of such a cascade is not the same as the product of each system's transfer. This is due to the general 3-D nature of the resulting image (a 3-D object has its image also a 3-D distribution of intensity.) Blurring on the image plane is then the result of projecting the (3-D) image distribution onto the image plane. However, we have chosen to model the blurring two-stage process as is fairly conventional:

- a. Ideal image registration (geometric and radiometric) giving $I_0(\mathbf{x})$, the idealized unblurred image.
- b. Blurring with blur width depending on $\mathbf{u}(\mathbf{x})$, or the depth value of the point $P = (X, Y, \mathbf{u}(\mathbf{x}))$ that has its image at \mathbf{x} .

For the one-dimensional model in figure 1, we can see that, at each image coordinate value x_ν , the resulting intensity also contains the sum of all blurring (or diffusion) contribution from neighboring image regions (ie. pixels, etc.), each of which may have a different blurring kernel. Concisely, then:

$$I(x_\nu) = \sum_{j \in J} I_j(x_\nu); \quad (4)$$

where j indexes the different image components near x_ν .

For our 1-dimensional, 2-component case, in particular, let $x_\nu = 0$, and let the ideal image intensity levels from the edge and the background to be respectively I_{e0} , I_{b0} . The blurred components are $I_e(x)$, $I_b(x)$ such that:

$$\begin{aligned} I(x) &= I_e(x) + I_b(x) \quad : \quad 2 \text{ components} \\ I_e(x) &= \int_{-\infty}^{\infty} K_e(x, x') I_{e0} \xi(-x') dx' = \int_{-\infty}^0 K_e(x, x') I_{e0} dx' \\ I_b(x) &= \int_{-\infty}^{\infty} K_b(x, x') I_{b0} T_b(x') dx' \approx \int_{-\epsilon}^{\infty} K_b^*(x, x') I_{b0} dx' \end{aligned} \quad (5)$$

where $T_b(x)$, describing the lens occlusion effect due to the edge, is similar to a smeared step function. Typically, the occlusion effects is small, and an ideal step function $\xi(x)$ can be used for $T_b(x)$. Or, the background blurring kernel $K_b^*(x, x')$ is distorted from a simple $K_b(x, x')$. We will not go into details of the lens occlusion effect, which is secondary. See figures 1 and 10.

With the analogy between Gaussian blurring and heat diffusion [Hum85], [Per90], multi-component Gaussian blurring is analogous to multi-component *particle*

diffusion, whereas each type of particle has a different diffusion constant, and none of them react chemically with each other. Note that analogy with heat diffusion cannot be easily made, since temperature is a single entity, unless we distinguish between different types of heat (due to different causes, and propagate at different rates, for example.)

2.3 Emergence of image details by multi-component blurring effects

Continued from above, we now show that multi-component blurring can give rise to new image features (or details), as opposed to the consistent suppression of details by single-component blurring models. By new image details, we mean specifically new local extrema, ie. local peaks and valleys. Just for ease of blurring width estimation/verification later, we assume here that every component kernel is some shift-invariant Gaussian, but other unimodal kernels can be used.

The 1-dimensional unblurred image is again taken to be approximately two disjoint step functions with heights I_{e0} , I_{b0} . The blurred components are $I_e(x)$, $I_b(x)$ respectively.

$$\begin{aligned} I(x) &= I_e(x) + I_b(x); & I_{\text{unblurred}}(x) &= I_{e0}\xi(-x) + I_{b0}\xi(x); \\ I_e(x) &= G_e(x) * I_{e0}\xi(-x); & I_b(x) &= G_b(x) * I_{b0}\xi(x) \\ \xi(u) &= \begin{cases} 1; & u \geq 0 \\ 0; & u < 0 \end{cases} & \text{unit step function} \end{aligned} \quad (6)$$

Where * denotes convolution. Figures 2(a), 2(b) show the two components, and figure 2(c) and 2(d) show a resulting MCB profile with emergent extrema. Note that with ideal step functions as shown, a continuous, uni-modal single blurring kernel will not introduce new local extrema. (This is the maximum principle, a main assumption in the Gaussian scale-space concept [Per90], however, MCB does not obey such restrictions.) At the emergent extrema location x_z , the gradient vanishes:

$$\begin{aligned} \frac{\partial}{\partial x} (G_e(x) * I_{e0}\xi(-x) + G_b(x) * I_{b0}\xi(-x)) &= -I_{e0}G_e(x) + I_{b0}G_b(x) = 0; \\ \text{giving } \frac{1}{\sqrt{2\pi}} \left(\frac{I_{b0}}{\sigma_b} \exp\left(\frac{-x_z^2}{2\sigma_b^2}\right) - \frac{I_{e0}}{\sigma_e} \exp\left(\frac{-x_z^2}{2\sigma_e^2}\right) \right) &= 0; \\ \text{or } \frac{I_{b0}\sigma_e}{I_{e0}\sigma_b} &= \exp\left(\frac{x_z^2}{2}\right) \left(\frac{1}{\sigma_b^2} - \frac{1}{\sigma_e^2} \right); \end{aligned} \quad (7)$$

The resulting conditions and solution for x_z , are:

$$\begin{aligned} \text{if } (\sigma_e > \sigma_b) \text{ and } (\sigma_e I_{b0} < \sigma_b I_{e0}); \quad \text{or } (\sigma_e < \sigma_b) \text{ and } (\sigma_e I_{b0} > \sigma_b I_{e0}) \\ \text{then } x_z^2 &= \frac{2\sigma_e^2\sigma_b^2}{(\sigma_e + \sigma_b)(\sigma_e - \sigma_b)} \ln \left(\frac{I_{b0}\sigma_e}{I_{e0}\sigma_b} \right) \end{aligned} \quad (8)$$

Note that the MCB gradient profiles can be quite different from those of SCB (single-component blurring). See also figures 3(aa), 3(bb) 3(cc) and 3(dd). For some range of I_{e0} , I_{b0} , the MCB gradient actually is a weighted difference-of-gaussian, an interesting fact.

Examples: Figure 3 shows a comparison of multi-component Gaussian blurring effects (3(a), 3(b), 3(c), 3(d)) to the effects of comparable-width single-component

Gaussian blurring. Only I_{b0} is varied, with $I_{e0} = 190$, $\sigma_e=5$, $\sigma_b=3$. Values for I_{b0} are 210, 190, 150 and 105 respectively. The same set of I_{e0} , σ_e , and I_{b0} was used for single-kernel blurring (which has $\sigma_e = \sigma_b = 5$). It is quite evident that multi-component blurring is capable of creating new interesting *extrema*. Note also that, even though case 3(a) looks like *Mach-band* effect due to human retino-optic ganglion cells [Lev85] (or, in image processing, edge-enhancement schemes using filters similar to Laplacian-of-Gaussian kernels), *MCB effects are not results of any purposive image processing*. We are talking of images as registered onto the camera imaging sensor plane.

And there could be no confusion with Mach-band or edge-enhancement processing in cases like figures 3(b) and 3(c), because the “peak” can occur well below the “brighter” level (into the “darker” side, as long as the “dark” side is not too dark.) Specifically, with given image parameters, for new extrema to be created, I_{b0} must satisfy:

$$I_{b0} > \frac{\sigma_b}{\sigma_e} I_{e0} = 114 \quad (9)$$

which is larger than 105 (value of I_{b0} , the right image component in figure 3(d).) Hence in figure 3(d), no extrema emerged.

Physical limitations such as blooming and smear of the imaging sensor elements (pixels) [TI86] by the mechanism of charge spilling between adjacent pixels, also help to blur the intensity difference between neighbor pixels, thus softening MCB features somewhat. The net effect is that the local extrema by MCB are most detectable for some range of I_{e0}/I_{b0} , with some upper limits dictated by CCD sensor characteristics, and lower limits at least as high as given by equation (8). This suggests that, unlike usual blurring effects, MCB effects are more detectable at *lower* local contrast, a rather surprising prediction that was actually observed in real images, and have possible implications to human perception. See figures 11, 12, 13, 14, and especially figure 18.

Let us try to see what it takes for a *single* convolution kernel to describe well the blurring effects shown). Then, the resulting kernel $K_{\text{composite}}(x, x')$ is given by:

$$K_{\text{composite}}(x, x') = \begin{cases} G_b(x - x'), & x' \geq 0 \\ G_e(x - x'), & x' < 0 \end{cases} \quad (10)$$

which looks innocuously simple, until we see some sample plots of it in figure 4. As seen, with $\sigma_e=5$, $\sigma_b=3$, $K_{\text{composite}}(x, x')$ is neither Gaussian (it's a patching of 2 truncated Gaussian segments), nor shift-invariant, and not even continuous at $x'=0$ (blurring interface.) These characteristics are more pronounced for larger ratios between the blur widths σ_e , σ_b , and for smaller absolute values of x_z . MCB blurring can be very complex to estimate, because even for the simpler case of shift-invariant single Gaussian blurring (directly analogous to heat diffusion) we cannot get exact inverse solution (ie. for deblurring or estimation of the blur width.)[Hum85]

Note that even with anisotropic diffusion (blurring) model [Per90], new details (new local extrema) cannot be created (by the maximum principle), only that some existing details can be preserved and possibly enhanced (ie. sharpened.)

3 Study on Real Camera Images

From the above model for MCB, we set out to experiment with real images to test the hypothesis that MCB effects do exist and can be detected in images of realistic scenes.

3.1 Experimental setup

The set up is quite similar to the imaging model in figure 1. Distances from camera are: 1.33 meters to edge of board **E**, and 5.69 meters to the 3 card boards that served as background **B** on the wall. The three background boards have slightly different reflectivities, thus enabling convenient investigation of MCB effect due local contrast (see figure 3 and figures 13, 14.) To make sure that other phenomena different than MCB blurring (de-focussing) were excluded from registering onto the images, we have insisted that: [Ngu90a]

- a. No specular reflections were present on or nearby the visible surfaces in the scene.
- b. No shadowing of the background patch **B** by the edge **E**.
- c. No interreflections (or mutual illuminations) between the two. Interreflections (mutual illuminations) between edge **E** and background **B** can give spurious details (local extrema) rather easy to be confused with MCB effects. See [For89].
- d. Illuminations had low partial coherence. See [Gla88].
- e. Image noise was reduced to about less than 1 gray level in variance, by temporal averaging of each image by 20 frames. This is also good for suppressing any noise due to the neon flicker.

3.2 Image data

Since a work of this nature must be extensively tested with carefully controlled experiments, we have performed extensive experiments (over 300 image frames taken for tens of scene set-ups) with consistent results. Here we included three typical sets of images and their video scan lines for further discussions. Note that all middle scan lines go through the medium-sized background card board.

- Set $\{M\}$ (figures 5 through 8) contains M_0 , an image of overall scene, and M_1 , M_3 , two images of the background (three patches) **B** (one close-up and one distant), and also M_2 , close-up image of edge **E**. This set serves to check for uniformity of **B** and **E** *both separately and together*. Note especially the “edge sharpness” and surface smoothness of the edge **E**.
- Set $\{N\}$ contains N_1 (figure 9), N_2 (figure 10). The parameter sets for them are back-focal distance, aperture diameter, and focal length, respectively (\mathbf{v} , \mathbf{D} , \mathbf{f}):
 - N_1 with $(\mathbf{v}, \mathbf{D}, \mathbf{f}) = (6375 \text{ mf}, 7420 \text{ ma}, 8760 \text{ mz})$ or $(87 \text{ mm}, 4 \text{ mm}, 84 \text{ mm})$.
 - N_2 taken with $(\mathbf{v}, \mathbf{D}, \mathbf{f}) = (6375 \text{ mf}, 9450 \text{ ma}, 8760 \text{ mz})$ or $(87 \text{ mm}, 6 \text{ mm}, 84 \text{ mm})$.

All parameters are expressed in machine units corresponding to the zoom lens digital controller readout: focus (mf), aperture (ma) and zoom (mz). Corresponding physical values of $(\mathbf{v}, \mathbf{D}, \mathbf{f})$ are believed to be only accurate to within 5 percent, due to lack of precise radiometric calibration for aperture (which is a complex entity for any zoom lens.)

- Set $\{P\}$ has P_1 (figure 11) and P_2 (figure 12) showing the MCB effects when camera parameters are fixed but scene lighting changed non-uniformly (so that local contrast can be controlled.) *Both* were taken with $(\mathbf{v}, \mathbf{D}, \mathbf{f}) = (6375 \text{ mf}, 9450 \text{ ma}, 4200 \text{ mz})$ or $(48 \text{ mm}, 6 \text{ mm}, 46 \text{ mm})$, but P_2 with a reduction in foreground lighting (which illuminates the edge **E**), which did not affect background lighting significantly since whole room was lit with 44 neon tubes

and only 2 small lamps (~ 100 watts each) were used for independent illumination of **E**.

To estimate independently the blurring widths of the background and the front edge, (so that we can compare MCB model with real image blurring effects due to depth discontinuity), we followed the simple method of Subbarao [Sub88b]. The blur widths (σ_e , σ_b) estimated in (horizontal) pixels were found as follows:

- a. For N_1 , approximately (3.23, 2.62)
- b. For N_2 , approximately (3.92, 3.45* (better fit with 3.0 due to lens occlusion))
- c. For P_1 , P_2 , approximately (2.08, 1.66)

Accounting also for video digitizer resampling, the effective pixel size is approximately $16.5\mu\text{m}$ (horizontal) by $13.5\mu\text{m}$ (vertical).

3.3 Interpretations

Refer to the figures 9 through 14. All images are originally 512×512 pixels but only central 500×420 image portion shown, and image coordinates (x , y) denote the original column and row indices, left to right and top to bottom. Analyses are done on horizontal slices at $y = 270$, called middle slices. The point $x = 243$ on all slices is at approximately "the interface" (corresponding to $x=0$ in figure 1) between the image regions of the background $\{x > 243\}$ and the edge $\{x \leq 243\}$.

The middle slices for the "ground-truth" images $M0$, $M1$, $M2$, $M3$ (controlled set), included with the images (figures 5 to 8), show negligible MCB effects. They reveal nothing very interesting on the background surface, nor across the depth discontinuity (figures $M0$ and $M2$.) Even right at the edge in image $M2$, one can only see a small dip in intensity mainly due to the remaining small roughness of the hand-cut (which absorbed and scatter lighting a little more.) However, the thin-lined curve in figure 5, which is the middle slice of image $M0^*$ (taken with same focal length as for $M0$, but with back-focus set so that edge **E** is blurred) demonstrates significant MCB blurring. However, $M0$ it self (dark dots) shows no such interesting feature.

Middle slices for images N_1 and N_2 (figures 9 and 10) reveal MCB effects with rather broad spatial extents, again near $x = 243$. For this image pair N_1 and N_2 , since the intensity ratio I_e/I_b is approximately unity (very low local contrasts), the MCB effects are controlled by w_b and w_c . Note also the persistence of MCB effects even with reduced aperture: overall intensities in N_1 is lower, but the "MCB details" still very pronounced. Compare these image slices to figures 3(a) through 3(d). Image N_2 shows effects of aperture occlusion, that is, the best-fitting w_b , value of 3.0 (for background, $x > 243$) is significantly smaller than the unoccluded background blur width w_b (about 3.45 pixels, see section 3.2 above)

Middle slices of P_1 and P_2 (figures 11 and 12, whose close-ups are figures 13 and 14) illustrate the detectability of MCB effects as a function of local intensity contrast I_e/I_b . See also section 2.2. That is, when I_e/I_b is closer to unity (lower local contrast), MCB effects are more pronounced. This is also suggested in comparison of slices ($y = 86$) as well as ($y = 270$) of P_1 , P_2 : reduced I_e reveals the "MCB spike" unseen with brighter foreground (and hence higher local contrast)! This could imply that human depth-perception may be enhanced *naturally* by MCB effects in low-contrast, large depth-range scenes. Section 4.2 next discusses this point.

4 Some Implications from the MCB Blurring Effects

We like to discuss the MCB effects on depth-from-focus, and also touch briefly on some recent results on human blur perception, which seems to support our speculation that human depth perception could be enhanced in low-contrast, large depth-variation settings, due to the MCB effects that can be detectable. [Hes89] [Ngu90a&b].

4.1 MCB blurring and depth-from-blur (or depth-from-focus)

Both Pentland [Pen87&89] and Subbarao [Sub88a], and others had worked on local blur estimation as an approach to 3-D perception, and with considerable successes, especially the real-time implementation by Pentland, which was up to a few hundred times as fast as correspondence-based stereo, making the approach rather attractive in some cases [Pen89]. We particularly pay attention to Pentland's simple "local power estimator" method, which is fast and reasonably accurate for single-component blurring cases. The more careful matrix formulation in [Ens91] improved on depth-from-blur accuracy incrementally, possibly best so far, but did not account for MCB, either. Also, even though depth-from-best-focus approach, such as Krotkov's [Kro89] and others, is different from the depth-from-blur approach, our following analyses have important implications to both, while we discuss only the later.

We also presented here, however, two sets of MCB simulated data that does not follow these researchers' models of local blurring. The simulated data are in fact very similar to real image scan lines obtained and discussed in section 3. We show that Pentland's "power measure" can in fact increase with increasing blur widths in many cases of MCB blurring. In other words, Pentland's method (as well as other methods mentioned above) fails to measure MCB blur.

In a nutshell, Pentland's approach can be summarized as: given a sharp image I_{sharp} and a blurred image I_{blur} (blurred by σ_{blur} ; $\sigma_{\text{blur}} > \sigma_{\text{sharp}}$), one can take localized power estimates $F_{\text{sharp}}(\lambda)$ and $F_{\text{blur}}(\lambda)$ for two corresponding image patches. Then utilizing the relation: [Pen89]

$$\mathbf{k}_1 \sigma_{\text{blur}}^2 + \mathbf{k}_2 \ln(\sigma_{\text{blur}}) + \mathbf{k}_3 = \ln(F_{\text{sharp}}(\lambda)) - \ln(F_{\text{blur}}(\lambda)) \quad (11)$$

one can estimate σ_{blur} given σ_{sharp} .

We take our typical scene a step edge blurred by a small Gaussian of width $\sigma_{\text{sharp}} = 1$, σ_{blur} varying from 1 to 6. For clarity, only images with $\sigma_{\text{blur}} = \{1, 3, 6\}$ are shown in figures 15(a), 16(a) and 17(a). Figure 15 illustrates the case of single-component blurring. The Pentland's power estimator applied to such a step edge of widths $\sigma_{\text{blur}} = \{1, 2, 3, 4, 5, 6\}$ gives power estimates (figure 15(b)). Then takes the difference of the logarithm, or logarithm of the ratio, of the power estimates. Points giving power ratios smaller than 1 are discarded. For single Gaussian blurring, the power responses dies off monotonically with increasing blur (figure 15(b)), giving a monotonically increasing power difference (figure 15(c)). For the Pentland's estimator shown in figure 15(c), median fitting was used for general robustness, though more refined approach can be used. Only mask size of 8 is used for the Laplacian-of-Gaussian and the Gaussian windows here, but similar results are obtained for larger windows.

Figures 16(b) and 17(b) show the results of trying to measure the "local power" of MCB edges, that have $\sigma_{\text{sharp}} = 1$ fixed on one side (left side in figure 16 and right side in figure 17), and the other side blurred with $\sigma_{\text{blur}} = \{1, \dots, 6\}$. Note the two

different manifestations of MCB blurring. Power measures for image set in figure 16 mostly increase with larger blur widths, except perhaps for a small range around $\sigma_{\text{blur}}/\sigma_{\text{sharp}} < 3$. Consequently, Pentland's model cannot be applied for reliable determination of σ_{blur} from these "power data".

Figure 17 gives not even a single case of valid power difference measure. This is because for all $\sigma_{\text{blur}} = \{1, \dots, 6\}$, the "image power" consistently increases with blur width, completely opposite to SCB case in figure 15(b). That is, the more blurring occurred, the higher the power measure. This last data set, as well as most of those from figure 16, defies any "local power estimation" approach, due to emergent high frequencies. We believe a gradient-based approach to be more viable.

4.2 MCB blurring effects and human blur perception

During the work in 1989 and published in [Ngu90b], we had speculated that MCB effects could play some important role in human visual perception, especially depth perception at low local contrast. This is a hypothesis arising naturally from the observations in section 3.3 on the characteristics of the MCB effects (emergent extrema). However, we had been unaware of any psychophysical data in favor of our hypothesis until recently when we found a paper by Hess [Hes89], who argued:

- a. that human blur discrimination (between blur edges slightly differing in blur extent) may actually rely more on low-frequency information, rather than high-frequency, near the vicinity of the blur edge transition.
- b. that discrimination is consistently enhanced if one of the blur edges is pre-processed so as to give an effect similar to MCB effects (he called phase-shifted processing instead), that is, very similar to figures 3(d), 13(a), and 14(a). For comparison, see figure 18, which contains our reproduction of his figures 10 and 11 in [Hes89].

The above conclusions came from Hess's study on blur discrimination *without* any depth information. Human subjects looked at computer-generated 2-D intensity profiles on a screen. [Wat83] However, conclusion (b) above was very favorable in support of our hypothesis, which also involves depth. We strongly believe that further investigation into human perception of blurring effects due to depth discontinuities could provide yet more clues into the working of human visual functions.

5 Discussions and Conclusions

In this paper, we have analyzed mainly the forward problem of multi-component blurring (MCB), discussed possible implications, and suggested that a gradient-based approach to the inverse problem could be promising. To summarize, we have:

- presented a simple but sufficiently accurate multi-component blurring model to describe blurring effects due to large depth discontinuities. Our model with aperture occlusion (section 2.2) is more general than a computer graphics (ray-tracing) model by Chen [Che88]. Due to space limitation we have restricted experimental verification to 1-D profiles.
- illustrated that current depth-from-blur algorithms could fail when significant MCB effects are present. Effects due to MCB blurring seemed to be ignored, or treated mistakenly like noise, by previous depth-from-focus algorithms [Pen89, Sub88, Ens91], which would give inaccurate depth estimates (averaging of estimates

mainly serves redistribution of errors) and unknowingly discard valuable depth information in MCB features.

□ raised an interesting speculation that MCB effects could play an important role in human depth perception, especially if the scene has low texture, low local contrast and large depth discontinuities. While we are not aware of any depth-from-blur experiment with human perception, we can point out some important recent results in human (2-D) blur perception [Hes89] that correlates well with the MCB effects presented here. Finally, although MCB effects are *definitely* not due to Mach-band illusion, the similarity between Mach-band and MCB effects in some cases could have led people to overlook the MCB effect in real images (thinking Mach-band effects were at work.) See [Lev85].

References

- [Che88] Chen, Y. C., "Synthetic Image Generation for Highly Defocused Scenes", *Recent Advances in Computer Graphics*, Springer-Verlag, 1988, pp. 117-125.
- [Ens91] Ens, J., and Lawrence, P., "A Matrix Based Method for Determining Depth from Focus", *Proc. Computer Vision and Pattern Recognition* 1991, pp. 600-606.
- [For89] Forsyth, D., and Zisserman, A., "Mutual Illuminations", *Proc. Computer Vision and Pattern Recognition*, 1989, California, USA, pp. 466-473.
- [Fri67] Frieden, B., "Optical Transfer of Three Dimensional Object", *Journal of the Optical Society of America*, Vol. 57, No. 1, 1967, pp. 56-66.
- [Gar87] Garibotto, G. and Storace, P. "3-D Range Estimate from the Focus Sharpness of Edges", *Proc. of the 4th Intl. Conf. on Image Analysis and Processing* (1987), Palermo, Italy, Vol. 2, pp. 321-328.
- [Gha78] Ghatak, A. and Thyagarajan, K., *Contemporary Optics*, Plenum Press, New York, 1978.
- [Gla88] Glasser, J., Vaillant, J., Chazallet, F., "An Accurate Method for Measuring the Spatial Resolution of Integrated Image Sensor", *Proc. SPIE Vol. 1027 Image Processing II*, 1988, pp. 40-47.
- [Gro87] Grossman, P., "Depth from Focus", *Pattern Recognition Letters*, 5, 1987, pp. 63-69.
- [Hea87] Healey, G. and Bindford, T., "Local Shape from Specularity", *Proc. of the 1st Intl. Conf. on Computer Vision (ICCV'87)*, London, UK, (1987), pp. 151-160.
- [Hes89] Hess, R. F., Pointer, J. S., and R. J. Watt, "How are spatial filters used in fovea and parafovea?", *Journal of the Optical Society of America*, A/Vol. 6, No. 2, Feb. 1989, pp. 329-339.
- [Hum85] Hummel, R., Kimia, B. and Zucker, S., "Gaussian Blur and the Heat Equation: Forward and Inverse Solution", *Proc. Computer Vision and Pattern Recognition*, 1985, pp. 668-671.
- [Kro89] Krotkov, E. P., *Active Computer Vision by Cooperative Focus and Stereo*, Springer-Verlag, 1989, pp. 19-41.
- [Lev85] Levine, M., *Vision in Man and Machine*, McGraw-Hill, 1985, pp. 220-224.

[Ngu90a] Nguyen, T. C., and Huang, T. S., "Image Blurring Effects Due to Depth Discontinuities", *Technical Note ISP-1080*, University of Illinois, May 1990.

[Ngu90b] Nguyen, T. C., and Huang, T. S., "Image Blurring Effects Due to Depth Discontinuities", *Proc. Image Understanding Workshop*, 1990, pp. 174-178.

[Per90] Perona, P. and Malik, J., "Scale-space and Edge Detection using Anisotropic Diffusion", *IEEE Transactions on Pattern Analysis and Machine Intelligence*, Vol. PAMI-12, No. 7, July 1990, pp. 629-639.

[Pen87] Pentland, A., "A New Sense for Depth of Field", *IEEE Trans. on Pattern Recognition and Machine Intelligence*, Vol. PAMI-9, No. 4 (1987), pp. 523-531.

[Pen89] Pentland, A., Darrell, T., Turk, M., and Huang, W., "A Simple, Real-time Range Camera", *Proc. Computer Vision and Pattern Recognition*, 1989, pp. 256-261.

[Sub88a] Subbarao, M., "Parallel Depth Recovery by Changing Camera Parameters", *Proc. of the 2nd Intl. Conf. on Computer Vision*, 1988, pp. 149-155.

[Sub88b] Subbarao, M., "Parallel Depth Recovery from Blurred Edges", *Proc. Computer Vision and Pattern Recognition*, Ann Arbor, June 1988, pp. 498-503.

[TI86] Texas Instruments Inc., *Advanced Information Document for TI Imaging Sensor TC241*, Texas, August 1986.

[Wat83] Watt, R. J., and Morgan M. J., "The Recognition and Representation of Edge Blur: Evidence for Spatial Primitives in Human Vision", *Vision Research*, Vol. 23, No. 12, 1983, pp. 1465-1477.

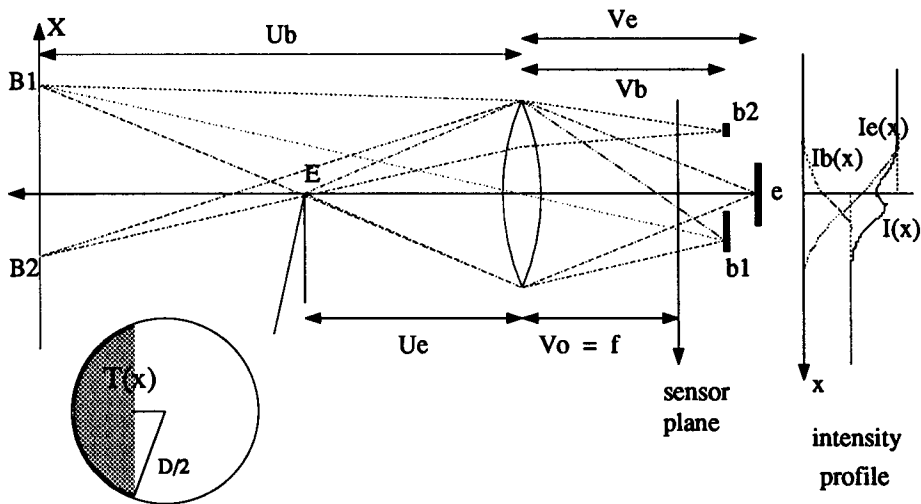


Figure 1. Imaging a sharp discontinuity: model for experimental set-up. Camera is focused at infinity. The dark segments near points e , $b1$, $b2$ illustrate relative sizes of blurring widths. $T(x)$ describes the lens occlusion effects (see figure 10, image $N2$) for some background points like point $B2$. If background B is very far, $T(x)$ can be replaced by a simple on-off model (hence, the simple step image profile.)

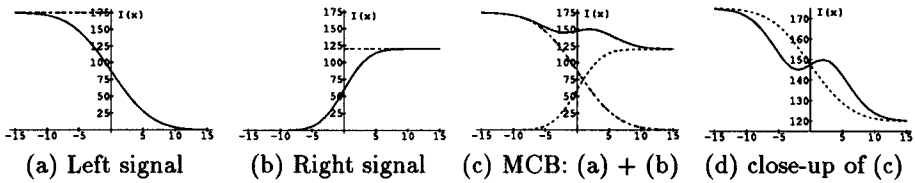


Figure 2. Example of a 1-D step edge with a two-component MCB. $\sigma_{\text{left}}=5$, while $\sigma_{\text{right}}=3$. The kernels are all Gaussian. Figure 2.(d) compares the resultant MCB profile with a single-component Gaussian blurring with $\sigma = 5$.

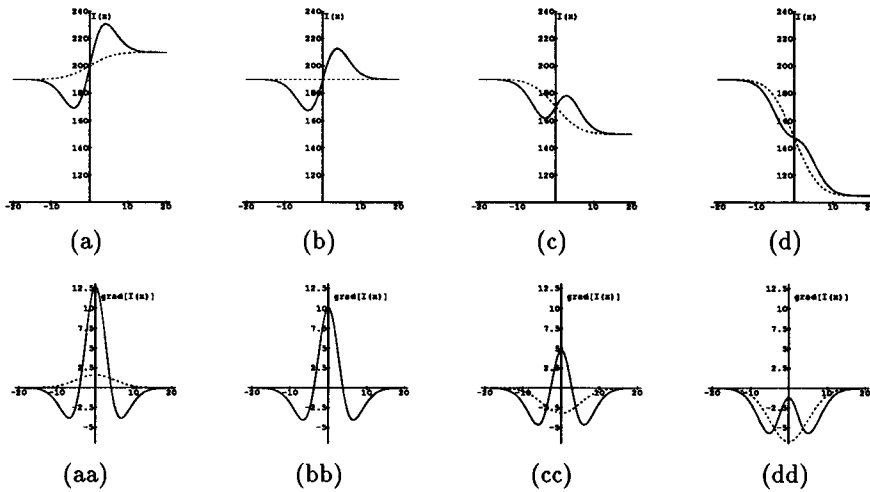


Figure 3. (a), (b), (c), (d) show Gaussian MCB and SCB (dashed) profiles in comparison. For MCB case, $\sigma_{\text{left}} = 5$, $\sigma_{\text{right}} = 3$, as in figure 2. Figures 3. (aa), (bb), (cc), (dd) shows the corresponding MCB and SCB gradient profiles in comparison. Discussion in section 2.2.

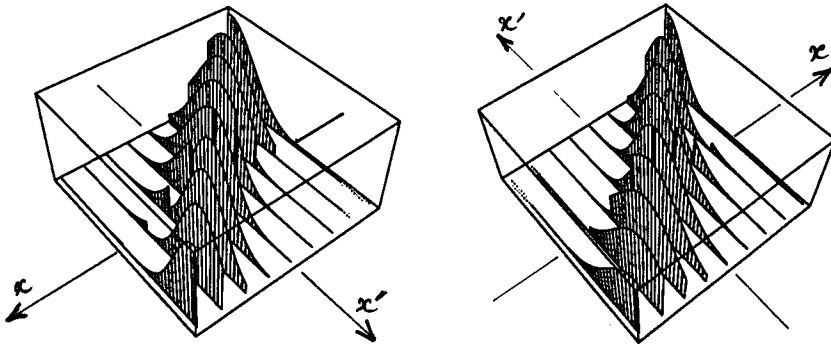


Figure 4. Two views of the $K_{\text{composite}}(x, x')$ composite blurring kernel for figures 2 and 3 above. See equation 10 in section 2.3.

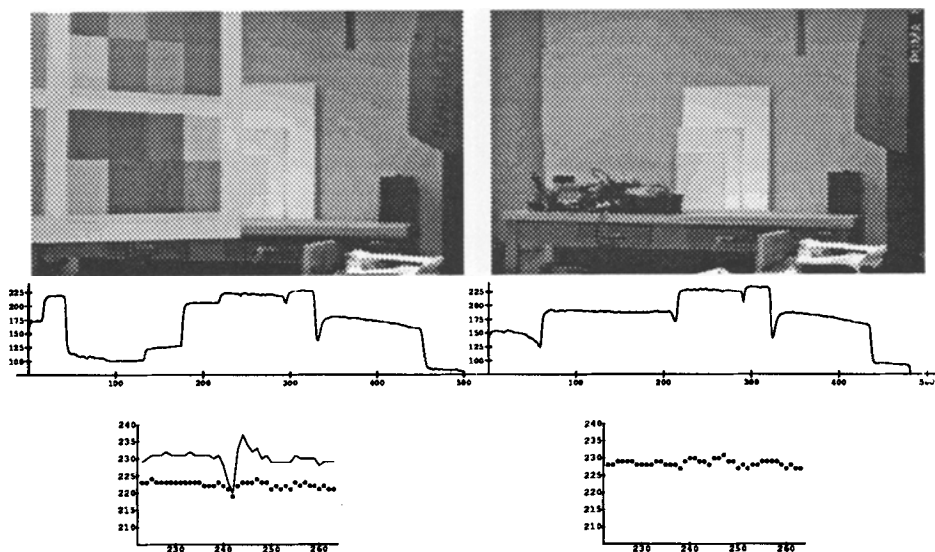


Fig. 5 Image M0: setup (Section 3.3)

Fig. 6 Image M1: background patches

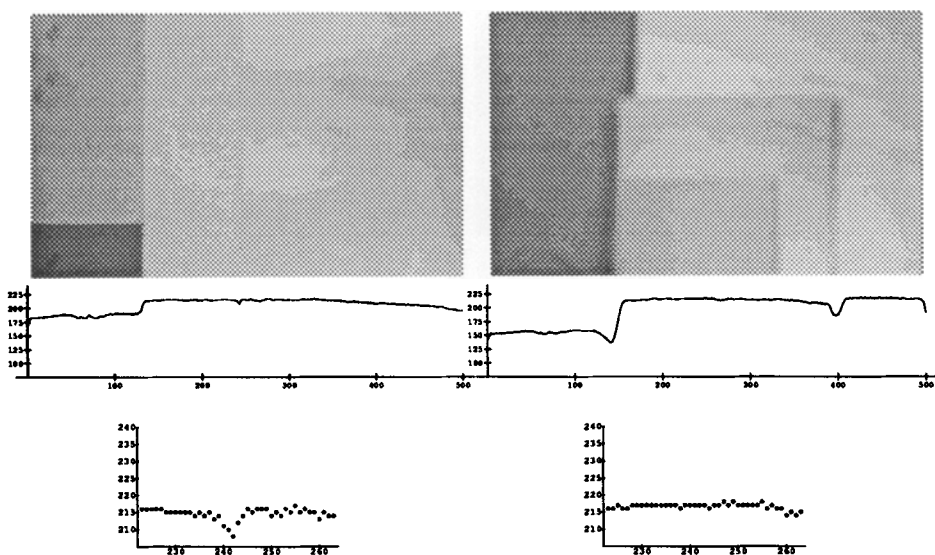


Fig. 7 Image M2: Close-up of the edge

Fig. 8 Image M3: Close-up of background

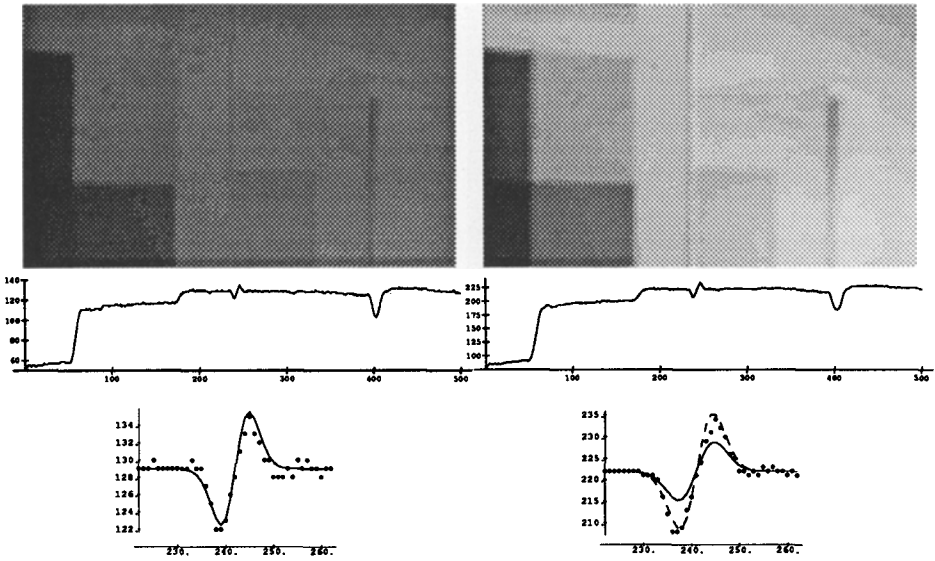


Fig. 9 Image N1: low local contrast

Fig. 10 Image N2: lens occlusion effect

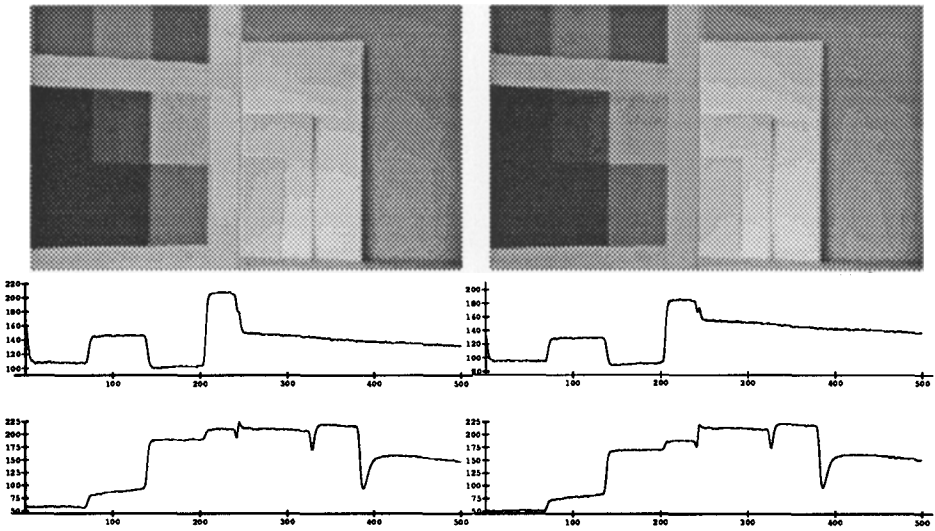


Fig. 11 Image P1 with row 86 and 270

Fig. 12 Image P2 with rows 86 and 270.

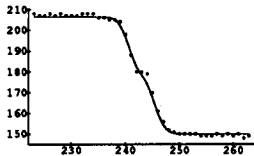


Fig. 13(a) Closed-up row 86 of P1

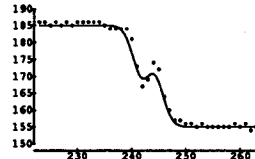


Fig. 14(a) Closed-up row 86 of P2

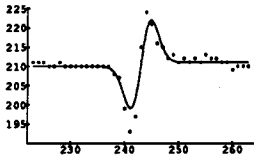


Fig. 13(b) Closed-up row 270 of P1

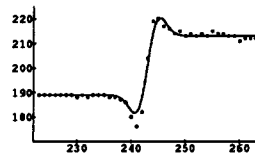


Fig. 14(b) Closed-up row 270 of P2

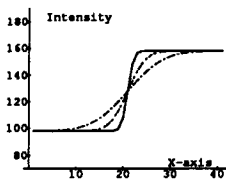


Fig. 15(a)

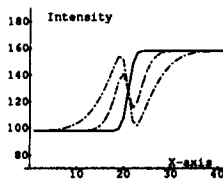


Fig. 16(a)

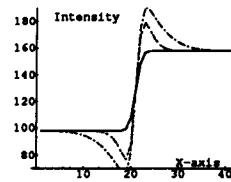


Fig. 17(a)

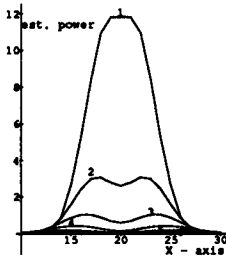


Fig. 15(b)

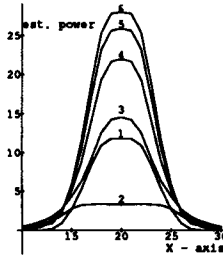


Fig. 16(b)

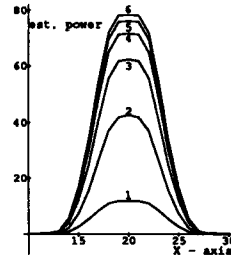
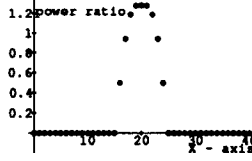


Fig. 17(b)



Fig. 15(c) Pentland's estimator



See section 4.1

No estimator: 16(b), 17(b)

For the MCB cases in the middle column (figure 16) Pentland's is of very limited use (the bottom row in middle column is the only valid "power image difference" between $\sigma_{\text{right}} = 1$ and $\sigma_{\text{right}} = 2$.) For MCB cases in the last column (figure 17) Pentland's method is inapplicable. See section 4.1. Note different power scales.

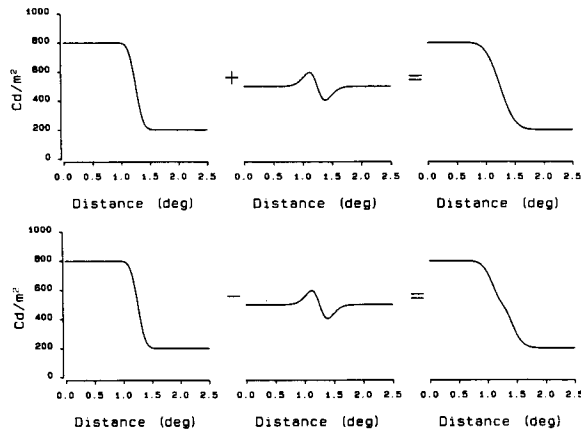


Fig. 10. Top row, two just-discriminable edges and their spatial difference. Bottom row, consequences of inverting the phase of this difference.

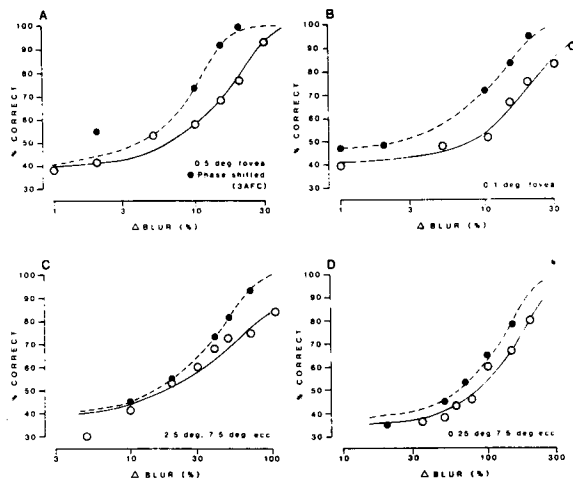


Fig. 11. Psychometric functions for blur discrimination between stimuli that have the same difference in their amplitude spectrum but with different phase spectra. Open symbols represent discriminations between the same edge stimuli discussed. Filled symbols represent discriminations between phase-shifted versions of the original stimuli (see the text). Results are given for a range of pedestal blurs and eccentricities. Note that the abscissa is a logarithmic scale, so that the factor by which discrimination is affected by this maneuver can be gauged. Solid curves are best fits to the data, obtained by using probit analysis. Discrimination between phase-shifted versions of the original stimuli are better by a factor of 2. This argues against a frequency filter code and argues for a space filter code (see the text).

Figure 18. Our reproduction of Hess and Pointer's results on blur discrimination.

The phase-shifted processing, second row of his figure 10, consistently enhanced human blur discrimination. Compare his figure 10 with our figures 3(d), 13(a), 14(a).